Chemical Engineering Journal 334 (2018) 2142–2153

Contents lists available at ScienceDirect

Chemical Engineering Journal

journal homepage: www.elsevier.com/locate/cej

Synergistic effects of 2D/2D ZnV_2O_6/RGO nanosheets heterojunction for stable and high performance photo-induced CO_2 reduction to solar fuels

Abdullah Bafaqeer, Muhammad Tahir*, Nor Aishah Saidina Amin

Chemical Reaction Engineering Group (GREG), Faculty of Chemical and Energy Engineering, Universiti Teknologi Malaysia, 81310, UTM, Johor Bahru, Johor, Malaysia

GRAPHICAL ABSTRACT

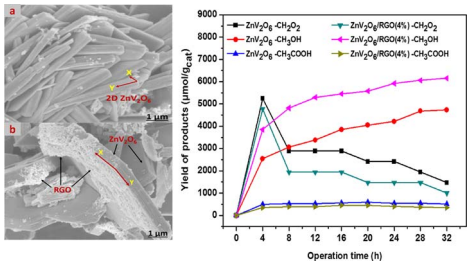

ARTICLE INFO

Keywords:
Novel ZnV_2O_6 nanosheets
2D/2D structure
RGO
CO_2 reduction
CH_3OH production
Visible light

ABSTRACT

Highly photo-stable and efficient 2D/2D zinc vanadium oxide-reduced graphene oxide (ZnV_2O_6/RGO) nanosheets heterojunction was fabricated by the one-pot solvothermal method. The structures and properties of the catalysts were analyzed by XRD, FE-SEM, EDX, TEM, BET, UV–vis, Raman and PL spectroscopy. The 2D/2D ZnV_2O_6/RGO catalyst shows excellent performance towards CO_2 photo-reduction with H_2O to CH_3OH, CH_3COOH and HCOOH under visible light. The yield of the main product CH_3OH of 5154 µmol g-cat^{-1}, obtained over ZnV_2O_6/4%RGO, was 1.6 times the amount of CH_3OH produced over the pure ZnV_2O_6 (3254 µmol g-cat^{-1}) and a 5.5-fold higher than that of the ZnO/V_2O_5 composite (945 µmol g-cat^{-1}). In addition, CH_3OH selectivity of 39.96% achieved over the ZnO/V_2O_5 composite increased to 68.89% in ZnV_2O_6/4%RGO. The continuous and selective production of CH_3OH was detected over the entire irradiation time in ZnV_2O_6 and ZnV_2O_6/4%RGO samples, whereas the yield of products gradually decreased in ZnO/V_2O_5. The significant improvement in photo-activity over 2D ZnV_2O_6 structure was due to the hierarchical structure with enhanced charges separation. A combined 2D/2D ZnV_2O_6/RGO nanosheets prevailed as a promising strategy to ameliorate the photocatalytic performance of ZnV_2O_6 nanosheets due to efficient trapping and transport of electrons by RGO. The synergistic effects in ZnV_2O_6/RGO 2D/2D nanosheets exhibited excellent photocatalytic stability, which prevailed even after 32 h of operation time for selective and continuous CH_3OH production. A proposed photo-induced reaction mechanism, corroborated with the experimental data, was also deliberated.

1. Introduction

Due to global warming caused by a remarkable increase of carbon dioxide (CO_2) emission into the atmosphere, it is currently a great challenge to convert CO_2 into valuable fuels [1,2]. Artificial photosynthesis process to convert CO_2 into useful carbon sources such as CO, HCOOH, HCHO, CH_3OH, and CH_4 is an attractive alternatives because of the demand for methods to recycle CO_2 as a natural resource [3–8]. The solar photocatalytic conversion of CO_2 into industrially beneficial compounds offers one prospective path [9,10]. Sunlight is

* Corresponding author.
E-mail address: mtahir@cheme.utm.my (M. Tahir).

https://doi.org/10.1016/j.cej.2017.11.111
Received 22 June 2017; Received in revised form 25 October 2017; Accepted 21 November 2017
Available online 22 November 2017

one of the most attractive strategies to convert CO_2 to value added fuels or chemical products [11–13]. Thus, many research efforts have been made to develop efficient photo-catalysts for the reduction of CO_2 to fuels such as TiO_2 [14–17], ZnO [18,19], CdS [20], Ta_2O_5 [21], $InTaO_4$ [22]. Among all, ZnO has been a widely-studied semiconductor because of its strong oxidation and reduction abilities. In addition, it is environmentally friendly, relatively cheap and can be grown in various nanostructures via cost effective methods [23–25]. However, because of its wide direct band gap energy (~3.2 eV), ZnO can only be activated by UV light, which cannot make full use of the incoming solar spectrum. Furthermore, it suffers through high rate of charges recombination, resulted in poor photocatalytic performance [26,27]. So, it is important to expand the absorption band of ZnO-based photo-catalyst towards visible light. To address these problems, many approaches have been made which include preparing quantized ZnO nano-crystallites [28], depositing noble metals [29–31], surface photo-sensitization [32], and forming carbon-based composites [33–36].

Graphene, as a new carbon material, is regarded as one of the most promising addictive for hybrid materials, because of its large theoretical specific surface area, excellent electron mobility, and high transparency [37,38]. Thus, it is believed to be an attractive approach to modify ZnO with RGO to obtain a promising photo-catalyst for enhanced CO_2 reduction. For example, graphene bonded with ZnO [39], TiO_2 [40], WO_3 [41], and CdS [13] composites have been widely investigated for the reduction of CO_2 to various chemicals and fuels. In addition, coupling ZnO with visible light responsive semiconductors can extend optical absorption towards the visible part of the spectrum. In this perspective, vanadium oxide (V_2O_5), an important transition metal oxide semiconductor (band gap ~2.3 eV), can be a good candidate for capturing visible light [42,43]. Furthermore, both zinc and vanadium are earth abundant, relatively economical, and can offer several oxidation states, which can render a broad range of redox reactions.

Lately, hierarchical nanostructures such as nanosheets, nanorods, or nanoplates have garnered enormous attention and demonstrated remarkable performances in energy storage, photovoltaic solar cells, photochemical, and other device applications [44,45]. Therefore, developing zinc-vanadium nanostructures could enhance both photoactivity and selectivity compared to ZnO/V_2O_5 composite. Recently, ZnV_2O_4 has gained attention because of its interesting structural changes at low temperatures [46]. Different nanostructures of ZnV_2O_4 have been reported like hollow spheres, clewlike hollow structures, nanosheets, and glomerulus nano/microspheres for various applications [46–49]. They have shown good charge–discharge performance in lithium ion batteries and a promising photo-catalyst. While keeping in view, the important role of spinel oxides in different applications, it is very crucial to improve new facile and cost effective routes for the fabrication of diverse morphologies of these nanostructures and to explore the potential as alternative energy storage materials for future applications. However, structured ZnV_2O_4 based photo-catalyst has never been reported for photo-induced CO_2 reduction application. Therefore, it is appropriate to explore hierarchical ZnV_2O_4 semiconductor for photocatalytic CO_2 reduction applications under solar energy. Furthermore, the construction of a semiconductor heterojunction has attracted a lot of attention because of its perfect effectiveness in developing the photocatalytic activity [50]. In this perspective, the graphene/Bi_2WO_6 composite has shown significantly enhanced photocatalytic activity compared with the bare semiconductors [51]. Similarly, enhanced photoactivity has been reported over rGO@CuZnO@Fe_3O_4 composite catalyst for photocatalytic CO_2 reduction to CH_3OH [52]. Recently, g-C_3N_4 (2D)/CdS (1D)/rGO (2D) dual interface heterojunction for excellent and stable visible light photocatalytic hydrogen generation has been reported [53]. It is therefore, highly desirable to construct ZnV_2O_6/RGO composite heterojunction to enhance photocatalytic reduction of CO_2 to solar fuels under visible light irradiation.

Herein, we successfully designed and synthesized novel 2D ZnV_2O_6 nanosheets and RGO modified ZnV_2O_6 2D/2D nanosheets heterojunction through a solvothermal process. The materials were investigated for photo-induced CO_2 reduction by H_2O to fuels under visible light irradiations. The 2D/2D ZnV_2O_6/RGO nanosheets demonstrated significantly enhanced photoactivity in comparison to pure ZnV_2O_6 nanosheets for converting CO_2 to CH_3OH, HCOOH and CH_3COOH. The enhanced photocatalytic activity was attributed to hierarchical structure of ZnV_2O_6 with hindered charges recombination rate by RGO. The effect of the content of graphene on photocatalytic activity ZnV_2O_6 nanosheets were investigated. The stability test to determine the life of new materials and reaction pathways were also deliberated.

2. Experimental

2.1. Preparation of novel 2D ZnV_2O_6 nanosheets

The ZnV_2O_6 nanosheets were prepared using a solvothermal method. Typically, 2.052 mmole of ammonium metavanadate [NH_4VO_3] dispersed in 20 ml of N,N-dimethyl formamide (DMF) was added into zinc acetate [$Zn(O_2CCH_3)_2$] and continuously stirred to obtain a homogenous solution. Oxalic acid dehydrated [$H_2C_2O_4{\cdot}2H_2O$] with oxalic acid to NH_4VO_3 ratio of 1:3 was added afterward. After being stirred for 30 min, the obtained solution was transferred into a 50 ml Teflon lined autoclave, which was maintained at 200 °C for 24 h and then cooled to room temperature naturally to get black colour product. The precipitates collected were washed for several times with absolute ethanol, then dried in air flow oven at 80 °C for 12 h. The as prepared ZnV_2O_6 were calcined at 550 °C for 3 h and efficiency between as prepared and calcined materials was compared. Different ZnV_2O_6 samples were prepared with exposure times of heating for 12 h, 48 h and 72 h using the same procedure.

2.2. Synthesis of RGO-modified ZnV_2O_6 (ZnV_2O_6/RGO) nanosheets

In a typical synthesis, 2.052 mmole of ammonium metavanadate [NH_4VO_3] was added into 20 ml of N,N-dimethyl formamide (DMF). After stirring for 10 min, zinc acetate [$Zn(O_2CCH_3)_2$] was added to above solution and suspension was stirred continuously to obtain a homogenous solution. Later, oxalic acid dehydrated [$H_2C_2O_4{\cdot}2H_2O$] was added by adjusting ratio of oxalic acid to NH_4VO_3 of 1:3. Afterwards, a certain amount of graphene oxide was added into the solution and stirred for another 30 min. Finally, the obtained solution was transferred into a 50 ml Teflon lined autoclave, maintained at 200 °C for 24 h and then cooled to room temperature. The black precipitates collected were washed several times with absolute ethanol, and then dried in an oven at 80 °C for 12 h. A series of ZnV_2O_6-RGO nanosheets with different weight ratios of GO nanosheets (2%, 4%) were obtained using the same procedure.

2.3. Material characterization

The crystalline structure was determined using X-ray diffractometer (Rigaku Smart Lab) with Cu-Kα radiation (λ = 0.154178 nm) operated at 40 kV and 30 mA. The XRD patterns were obtained with a scanning rate of 0.02° min^{-1} and scanning range of 3–100° of 2θ. The morphology and EDX mapping analysis of the samples was examined by field emission scanning electron microscopy (FE-SEM, ZEISS Crossbean 340). The high-resolution transmission electron microscope (HR-TEM) images were obtained in a transmission electron microscope (TEM, HITACHI HT7700). Nitrogen-adsorption–desorption isotherms were collected using Micromeritics ASAP 2020 at 77 K, after degassing the samples at 523 K for 4 h under vacuum and using the nitrogen flux. The BET surface area and pore diameters were calculated from the desorption branch of isotherms according to BJH method. Ultraviolet–visible (UV–vis) diffuse reflectance absorbance spectra were carried out on a Cary 100 Agilent UV–vis spectrophotometer equipped

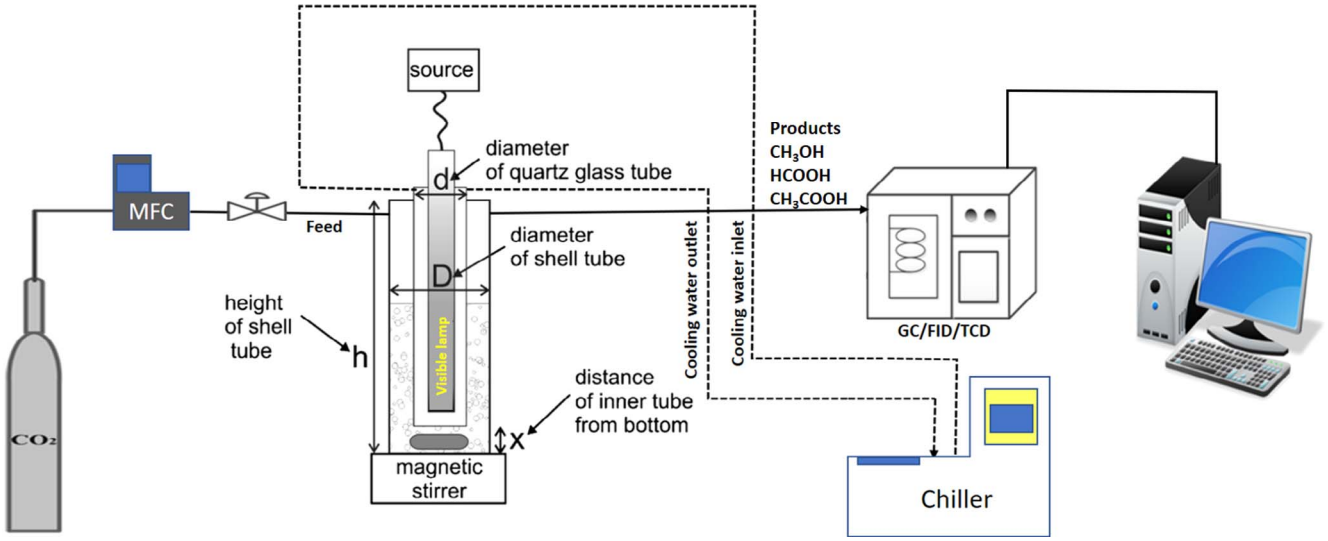

Fig. 1. Schematic of experimental set-up for CO_2 reduction in a slurry photoreactor system under visible light.

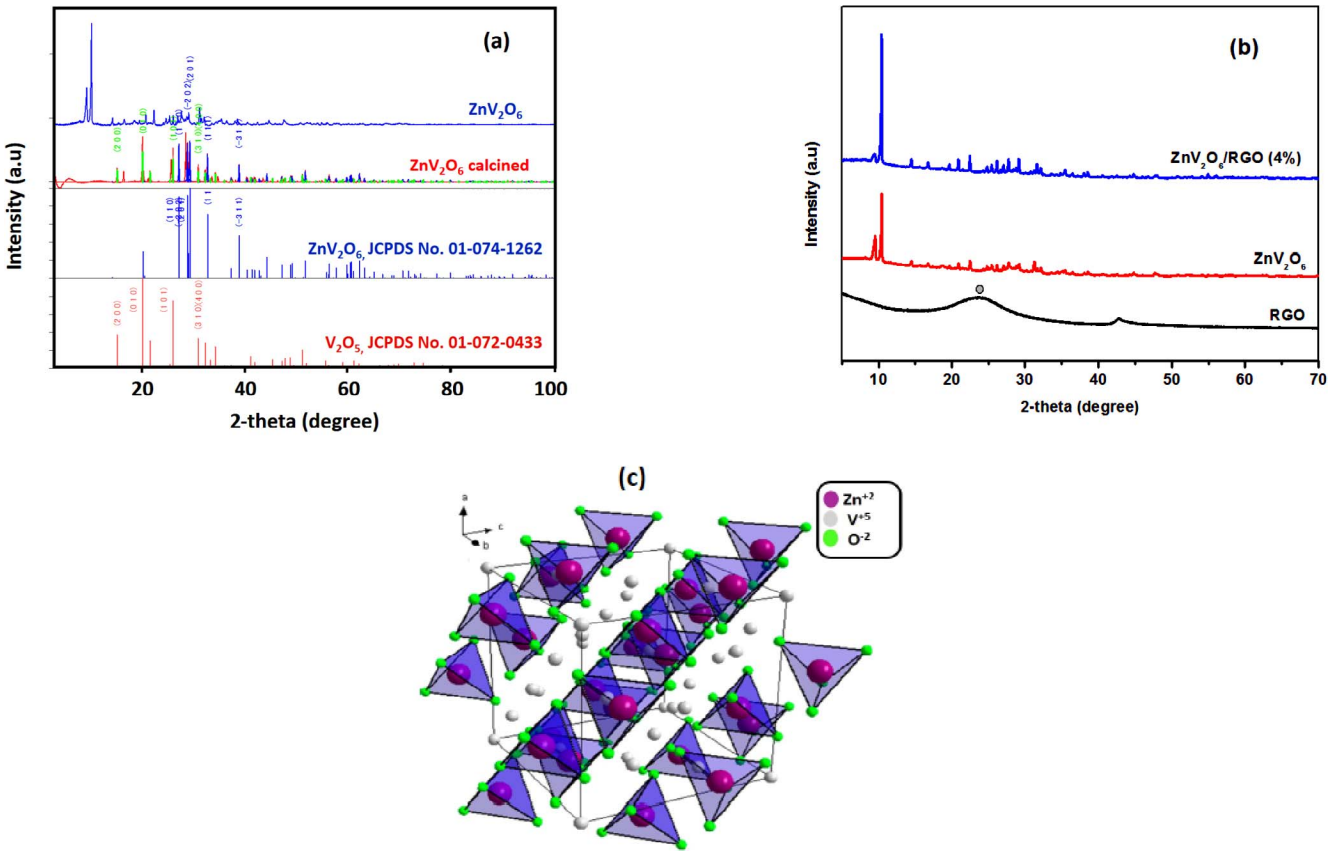

Fig. 2. XRD pattern of (a) ZnV_2O_6 and ZnV_2O_6 calcined and (b) RGO, ZnV_2O_6 and ZnV_2O_6/RGO samples, (c) Crystal structure of spinel ZnV_2O_6 with corresponding atoms (purple, white and green spheres represent zinc, vanadium and oxygen atoms, respectively).(For interpretation of the references to colour in this figure legend, the reader is referred to the web version of this article.)

with an integrated sphere in the wavelength range of 200–800 nm. Raman and photoluminescence (PL) spectra of the samples were recorded at room temperature using Raman Spectrometer (LabRAM HR Evolution, HORIBA), whereas, PL was conducted using 325 nm and Raman with a 532 nm emitting laser as an excitation source.

2.4. Photocatalytic activity

The schematic presentation of the slurry type photoreactor for CO_2 reduction is illustrated in Fig. 1. The CO_2 reduction reaction was performed using a quartz glass with a volume 100 ml. A 35 W HID Xe lamp was used as a visible light source with a light intensity of 20 $mWcm^{-2}$, measured using a reference solar cell (91150 V, Newport) [10]. First, 100 mg catalyst sample was added into 100 mL 0.1 M NaOH solution in a glass reactor under magnetic stirring. Then, compressed CO_2 regulated by mass flow controller (MFC) was bubbled through the solution for 30 min to remove the oxygen. The control experiments were conducted at room temperature, atmospheric pressure, and feed flow rate

of 20 mL/min. The HID XENON lamp was turned on to start the photoreaction. During the reaction process, the liquid products were taken out after 2 h interval, then were centrifuged using Syringe Filter with Nylon Membrane, pore size 0.45 μm and diameter 33 mm to remove catalyst particles. The concentration of methanol, formic acid and acetic acid were analyzed by a gas chromatograph (GC-7820A) equipped with a flame ionization detector (FID) and HP-5 capillary column. The calibration of the GC was conducted using standard solutions of methanol, formic acid and acetic acid. More importantly, methanol peaks areas obtained were consistent, yet peak areas for formic acid and acetic acid were different in different injections and their average values have been used for calibration curve. This happen because FID detector was not compatible for the analysis of these products. Control experiments were carried out in the dark or without catalyst under the same experimental conditions. The carbon containing products were not detected in the absence of light irradiation or catalysts.

3. Results and discussion

3.1. Characterization of catalysts

Fig. 2(a) shows XRD patterns of as synthesized and calcined ZnV_2O_6 samples. Clearly, the XRD pattern of the ZnV_2O_6 shows one pronounced diffraction peak located at around $2\theta = 10.0^\circ$. Such a diffraction pattern can be attributed to the ZnV_2O_6 phase, which is a characteristic of metal alkoxides [54,55]. The ZnV_2O_6 nanosheets were converted to highly crystalline material after calcining at 550 °C for 3 h in air atmosphere. All the identified diffraction peaks can be assigned to ZnV_2O_6 with an orthorhombic structure (JCPDS Card No. 01-074-1262). Also, weak diffraction peaks of V_2O_5 appeared, which indicated that a small amount of V_2O_5 (JCPDS Card No. 01-072-0433) was generated and the resulting sample was a mixture of ZnV_2O_6 nanosheets and V_2O_5. Fig. 2(b) displays an obvious diffraction peak at $2\theta = 25.0^\circ$ appears in the XRD patterns of RGO corresponding to the (0 0 2) reflection of reduced phase of graphene oxide. The XRD patterns of the ZnV_2O_6/RGO samples show similar diffraction patterns as ZnV_2O_6. The RGO peak is not observed in the composite, probably due to its lesser content. These results indicate that the introduction of RGO do not affect the orientation and structure of ZnV_2O_6 nanosheets.

Fig. 2(c) shows the interesting crystal geometry of spinel oxide ZnV_2O_6. The ZnV_2O_6 is formed by ZnO_4 tetrahedra and VO_6 octahedra. It belongs to the FCC type crystal structure with Fd3m symmetry group. According to crystallographic studies, zinc atoms reside in the tetrahedral 8a position, whereas the vanadium atoms are on 16d position, which forms a network of corner sharing tetrahedral structure. The oxygen ions are located at the 48e position.

The surface area (S_{BET}), pore volume and pore size of all samples are reported in Table 1. The BET surface area of 11.57 m^2/g for ZnV_2O_6 was obtained, obviously higher than the BET surface of ZnV_2O_4 of 6.1 m^2/g [56]. This was perhaps due to their different hierarchical structures. On the other hand, BET surface area of ZnV_2O_6 with 4 wt% RGO of 11.62 m^2/g obtained, which revealed RGO has no effect on the BET surface area of ZnV_2O_6. Moreover, pore diameter decreased with RGO-combined with ZnV_2O_6. Thus, the reduced pore diameter was possibly due to controlled crystal growth in the RGO-combined with ZnV_2O_6 samples. Therefore, well-developed mesoporous structure with larger pore volume and smaller pore diameter could minimize mass transfer limitations to increase catalyst activity.

Fig. 3 portrays the field emission scanning electron micrographs (FE-SEM) recorded in order to measure the morphology of ZnV_2O_6 and RGO-combined with ZnV_2O_6 2D/2D nanosheets. It can be seen in Fig. 3(a) that the ZnV_2O_6 sample prepared at 12 h reaction time composed of intermediate products which consists of many compact sheets. However, when the reaction time was increased to 24 h, large amounts of sheets were formed as shown in Fig. 3(b). Evidently, pure ZnV_2O_6 has

Table 1
Summary of physiochemical characteristics of photo-catalysts.

Sample	BET surface area S_{BET} (m^2/g)	BJH surface area S_{BJH} (m^2/g)	Pore volume (cm^3/g)	Pore width (nm)	Crystal size d_{xrd} (nm)	Band gap (E_{bg})
ZnV_2O_6	11.57	3.80	0.0045	17.30	1.355	2.02
ZnV_2O_6/RGO (4%)	11.62	10.48	0.0037	5.46	1.035	1.97

2D structure consisting of uniform size sheets with many wrinkles. Fig. 3(c and d) displays the micrograph of RGO sheets with a fold surface, the ZnV_2O_6 substrate is partly covered by the RGO nanosheets which reveals a good interaction between ZnV_2O_6 and RGO nanosheets.

The EDX mapping analysis are presented in Fig. 4. The EDX mapping analysis in Fig. 4(a and b) revealed even distributed of RGO over ZnV_2O_6 nanosheets. Zinc, vanadium, oxygen and carbon were the elements found by EDX analysis as shown in Fig. 4(c). The atomic ratio was found to be 18.3, 54.0, 22.0 and 5.6%, respectively. No other atom/elements were detected indicating purity of the product. These observation have confirmed successful development of RGO/ZnV_2O_6 composite heterojunction, which could results in enhanced photocatalytic activity.

The growth mechanism of the ZnV_2O_6/RGO nanosheets heterojunction is presented in Fig. 5. Initially, ZnV_2O_6 sheet intermediate product with compact nanosheets were formed in large quantity, which might provide the reaction sites and sources for the impending next step [49]. Besides, GO sheets will be distributed uniformly over the ZnV_2O_6 structure during the growth of 2D sheets. Rising the reaction time, abundant ZnV_2O_6/RGO sheets were generated by in situ reduction and continuous dissolution of the sheets intermediate product, and simultaneously aggregated into nanosheets to reduce surface energy. As the reaction proceeded in longer time, the nanosheets completely aggregated to regular nanosheets with relatively smooth surface of 2D/2D ZnV_2O_6/RGO heterojunctions.

The morphology and microstructures of the ZnV_2O_6/RGO nanosheets was characterized using TEM as depicted in Fig. 6. Fig. 6(a) shows the ultrathin RGO sheet has a highly transparent 2D structure with obvious wrinkles and folds. The TEM images of ZnV_2O_6 sample prepared after 24 h reaction time is presented in Fig. 6(b), which shows ZnV_2O_6 structure composed of many compact nanosheets. From Fig. 6(cand d) the RGO nanosheets are observed on the surface of ZnV_2O_6 nanosheets, which reveals a good combination of RGO and ZnV_2O_6 to develop heterojunction. HRTEM image in Fig. 6(e) illustrates that the RGO nanosheets are successfully deposited on the surface of ZnV_2O_6 nanosheets developing 2D/2D structure. This revealed the formation of heterojunction structure of the RGO/ZnV_2O_6 nanosheets. The interplaner distance was found to be 0.48 nm and 0.25 nm, which corresponds to (1 1 1) and (3 1 1) planes of ZnV_2O_6 nanosheets. The SAED pattern of the composite in Fig. 6(f) shows an obvious polycrystalline ring due to good crystallization of ZnV_2O_6. The calculated "d" values corresponds to (1 1 1) and (3 1 1) Miller indices of ZnV_2O_6.

Fig. 7 shows UV–vis diffuse reflectance absorbance spectra of the ZnO/V_2O_5 composite, pure ZnV_2O_6 and ZnV_2O_6/RGO nanosheets. The combined RGO with ZnV_2O_6 nanosheets can obviously enhance the absorbance of ZnV_2O_6 towards visible light irradiations. The energy band gaps (E_{bg}) of all the samples were obtained from the extrapolation of Tauc plot to the abscissa of photon energy (eV) and results are presented in Table 1. The wavelengths of the ZnO/V_2O_5, ZnV_2O_6 and ZnV_2O_6/RGO samples are 447 nm, 613 nm and 630 nm corresponding to the band gap energy of 2.77 eV, 2.02 eV, and 1.97 eV, respectively. Obviously, ZnV_2O_6 nanosheets displays higher absorption intensities than ZnO/V_2O_5 composite in the visible light region. Similarly, ZnV_2O_6/RGO nanosheets show slightly higher absorption intensities

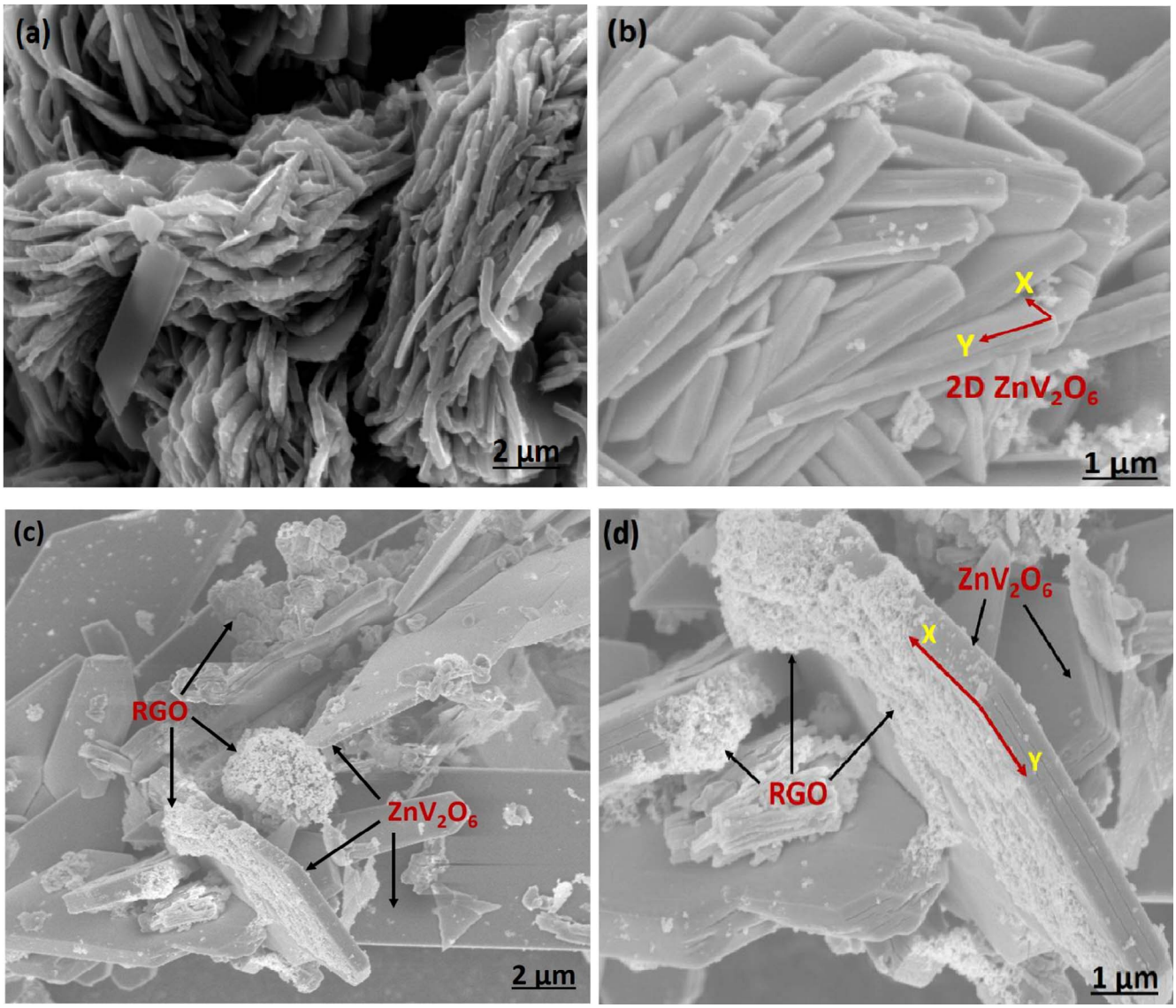

Fig. 3. FE-SEM images of (a) ZnV_2O_6 after 12 h, (b) ZnV_2O_6 after 24 h, (c, d) images of 2D/2D ZnV_2O_6/RGO (4%) nanosheets of different magnification.

than that of ZnV_2O_6 in the visible light region. The enhanced light absorption by RGO can be ascribed to the introduction of the black-body properties of graphene-like materials [51].

Raman spectra of the pure ZnV_2O_6 and RGO-combined with ZnV_2O_6 samples are depicted in Fig. 8(a). The Raman spectrum of the blank RGO contains both D (the symmetry A1g k-point phonon) and G (the E2g phonon of sp2 carbon atoms) bands at 1323 and 1581 cm^{-1}, respectively. The peaks in the range of 100–1100 cm^{-1} were observed in the pure ZnV_2O_6 sample. All the characteristic bands of the pure ZnV_2O_6 are found in the Raman spectrum of the ZnV_2O_6/RGO nanosheets, while, both the D and G bands disappeared due to its lesser content. However, the changes are obvious in the position and width of the combined ZnV_2O_6 sample peaks. With the RGO combined, the width of the Raman bands, in particular the peaks increase and the slight position shift towards higher wavenumber, attributed to the reduction of particle size of the combined ZnV_2O_6 samples with higher mobility of charges.

Fig. 8(b) shows photoluminescence (PL) spectra of the pure ZnV_2O_6 and RGO combined with ZnV_2O_6 samples. ZnV_2O_6 displays a broad PL emission peak at around 510 nm. The PL intensity of the pure ZnV_2O_6 exhibits the strongest emission due to the highest recombination of the photo generated charge carriers on the pure ZnV_2O_6 surface. After the RGO was introduced, the ZnV_2O_6/RGO nanosheets show lower PL emission intensity compared with the pure ZnV_2O_6. The weaker intensity of the peak represents the lower recombination probability of free charges [57]. This indicates that RGO can effectively mitigate the recombination of photo-generated electron hole pairs of ZnV_2O_6 nanosheets.

3.2. Photocatalytic CO_2 reduction with H_2O reductant

The control experiments were conducted in the presence of catalysts without CO_2 flow under visible light irradiation at room temperature, atmospheric pressure, and N_2 feed flow rate of 20 mL/min. In all the cases, carbon containing compounds were not detected, thus, any carbon based products would be produced during CO_2 reduction process only.

Fig. 9(a) displays the effect of different photo-catalysts such as ZnO, V_2O_5, ZnO/V_2O_5, ZnV_2O_6 and ZnV_2O_6 calcined on the photoactivity for dynamic CO_2 conversion with H_2O under visible light irradiation. The effectiveness of the catalyst samples were analysed based on the yield of CH_3OH, HCOOH and CH_3COOH which were the three products from the process. Pure ZnO, V_2O_5 and ZnO/V_2O_5 nanocatalyst synthesized by the sol–gel method scarcely reduced CO_2 and showed very poor activity

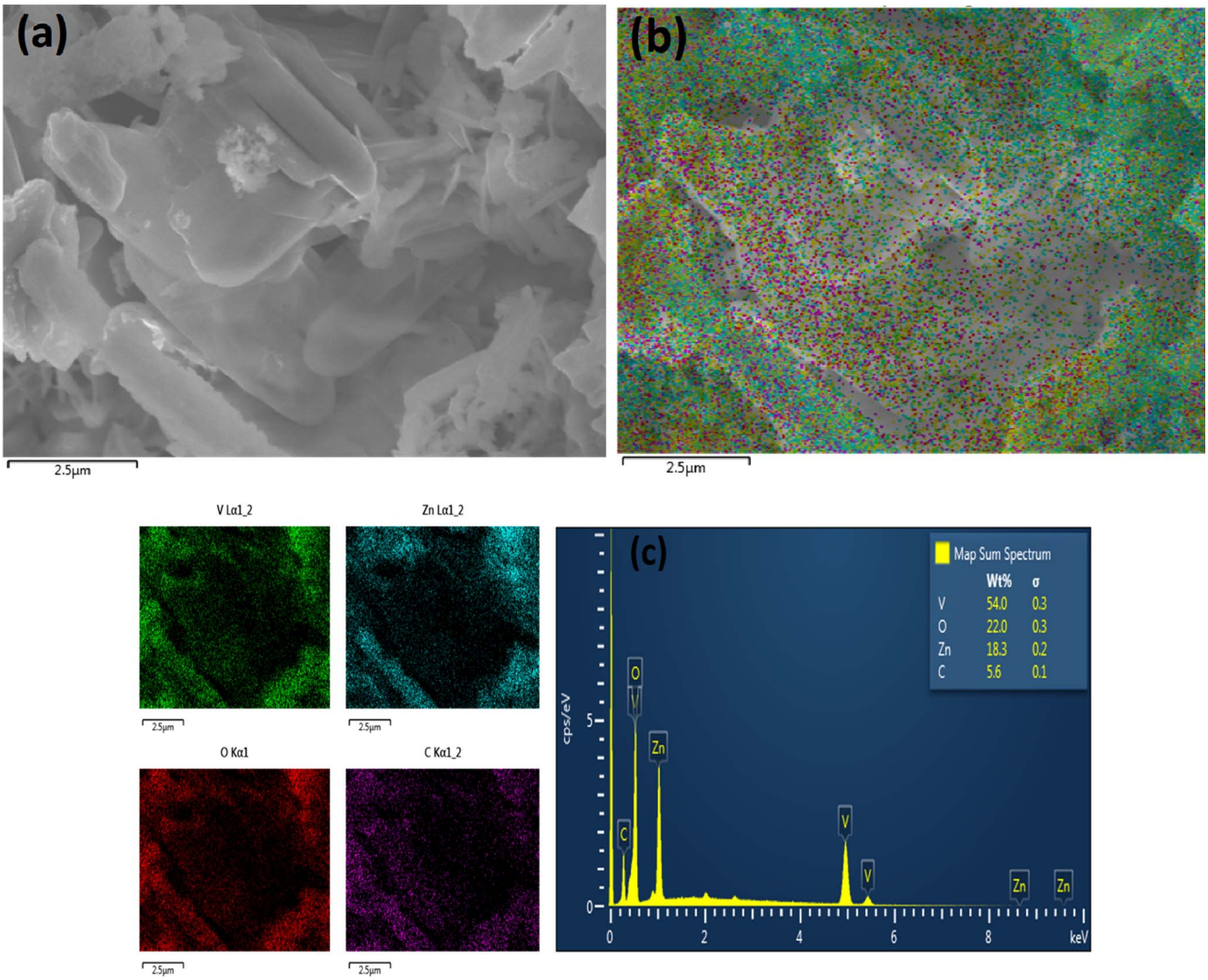

Fig. 4. EDX mapping analysis of RGO modified ZnV_2O_6 nanosheets: (a, b) EDX mapping of ZnV_2O_6/RGO, (c) EDX analysis of ZnV_2O_6/RGO sample.

for CH_3OH formation. However, the production of CH_3OH was significantly enhanced using novel 2D ZnV_2O_6 nanosheets due to efficient visible light absorption, efficient charge transfer property and higher electron mobility with hindered recombination rate by some amount of V_2O_5 in the sample as evidenced by XRD analysis [58]. More importantly, ZnV_2O_6 calcined at 550 °C for 3 h showed very poor activity under the same operating conditions. Recently, Zhang et al. [55] reported similar observations while investigating hydrogen evolution from water over $BiFeO_3$, $Bi_2Fe_4O_9$ and $BiFeO_3/Bi_2Fe_4O_9$ heterojunction nanofibers under visible light irradiation. Therefore, lower photo-activity of calcined ZnV_2O_6 sample was possibly due to change in morphology at elevated temperature. According to results, the production of CH_3OH in bare ZnV_2O_6 was much closer to calcined sample, yet it has an impact on the production of HCOOH and CH_3COOH. Therefore, further investigations would be required on understanding the possible reasons in lowering the photoactivity of calcined samples.

Fig. 9(b) shows the effect of different exposure times of heating for 12 h, 24 h, 48 h and 72 h for prepared ZnV_2O_6 catalyst for CO_2 photoreduction with H_2O under visible light irradiation in reaction medium (Room temperature, atmospheric pressure, feed flow rate 20 mL/min and irradiation time = 2 h). The results show that the effect of exposure time of heating for 24 h for prepared ZnV_2O_6 sample exhibits much higher CH_3OH, HCOOH and CH_3COOH evolution rate than heating time for 12 h. In particular, the evolution rate of products firstly increased with the exposure times of heating until 24 h, afterwards, there is not significant effect of exposure times of heating on ZnV_2O_6 catalyst photo-activity.

Further investigations were carried out to study the effect of irradiation time on dynamic photocatalytic CO_2 reduction in a slurry photoreactor. The production of CH_3OH and CH_3COOH gradually increased with increasing the time up to an optimum, whereas the HCOOH was decreased and then remained constant as shown in Fig. 10. Fig. 10(a) shows the yield of CH_3OH on ZnO/V_2O_5, ZnV_2O_6 and ZnV_2O_6/RGO catalysts under visible light irradiation. It can be seen that without RGO, pure ZnO/V_2O_5 and ZnV_2O_6 samples have a lower activity for CH_3OH production in the photocatalytic reduction of CO_2 compared with ZnV_2O_6 /RGO composite catalyst. After irradiation time of 10 h, CH_3OH yield of ZnV_2O_6/4% RGO (5153.97 µmol g-cat^{-1}) was about 5.5 times higher than that of pure ZnO/V_2O_5 (945.28 µmol g-cat^{-1}) and 1.6 times higher than that of pure ZnV_2O_6 (3253.84 µmol g-cat^{-1}). From the above results, graphene has a positive impact on the photocatalytic performance of ZnV_2O_6, which can be attributed to the synergetic effects between ZnV_2O_6 nanosheets and graphene nanosheets. This synergetic effect can improve the charge separation and the photocatalytic activity [59,60].

Fig. 10(b) presents HCOOH production over ZnO/V_2O_5, ZnV_2O_6 and ZnV_2O_6/RGO catalysts at different irradiation time. Obviously, HCOOH formation over ZnO/V_2O_5, ZnV_2O_6 and ZnV_2O_6/RGO presented a different behaviour, initially reaching maximum concentration, then gradually decreased. This declined in HCOOH production over the

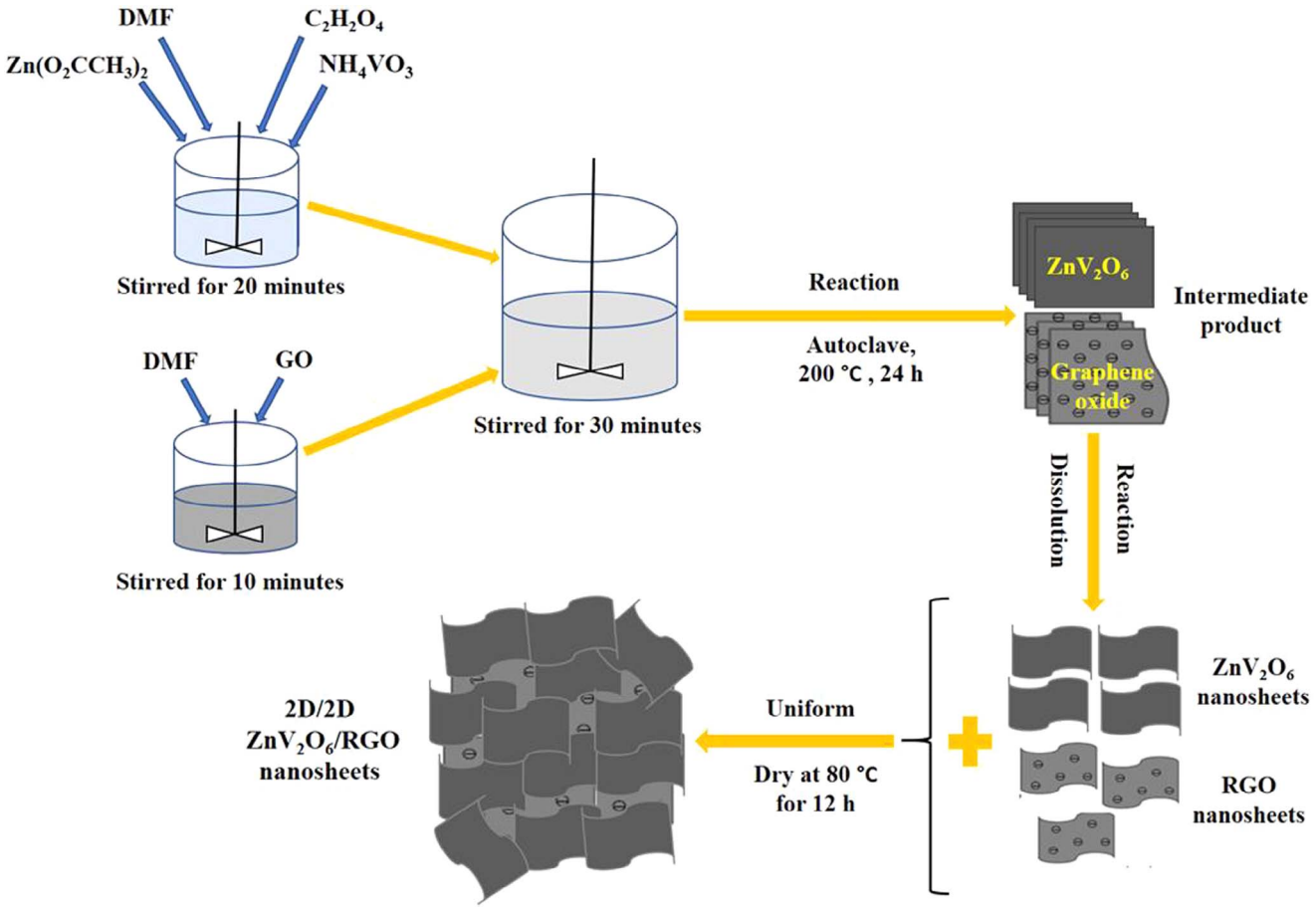

Fig. 5. Schematic illustration for the formation process of 2D/2D ZnV_2O_6/RGO nanosheets.

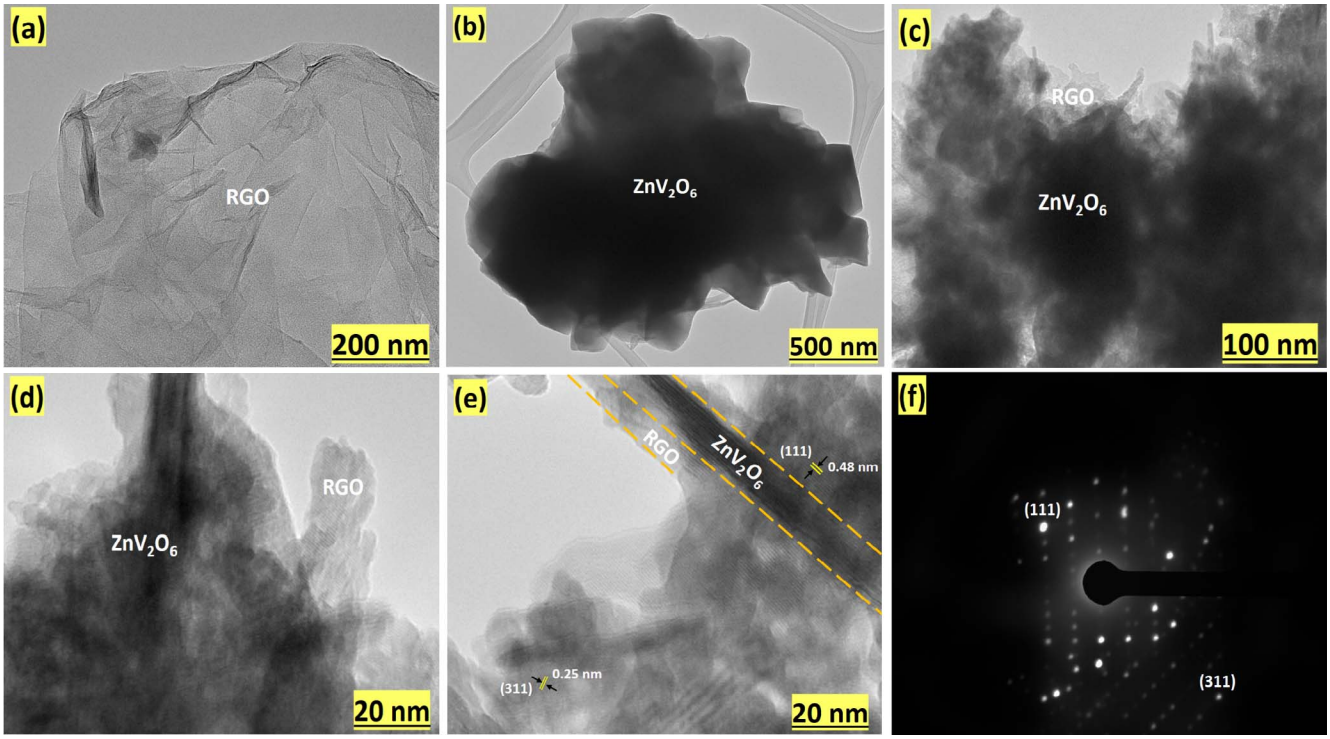

Fig. 6. (a) TEM image of RGO; (b) TEM image of 2D ZnV_2O_6 nanosheets; (c, d) TEM image of 2D/2D ZnV_2O_6/RGO (4%) nanosheets; (e) d-spacing of ZnV_2O_6/RGO sample, (f) SAED pattern of the corresponding sample.

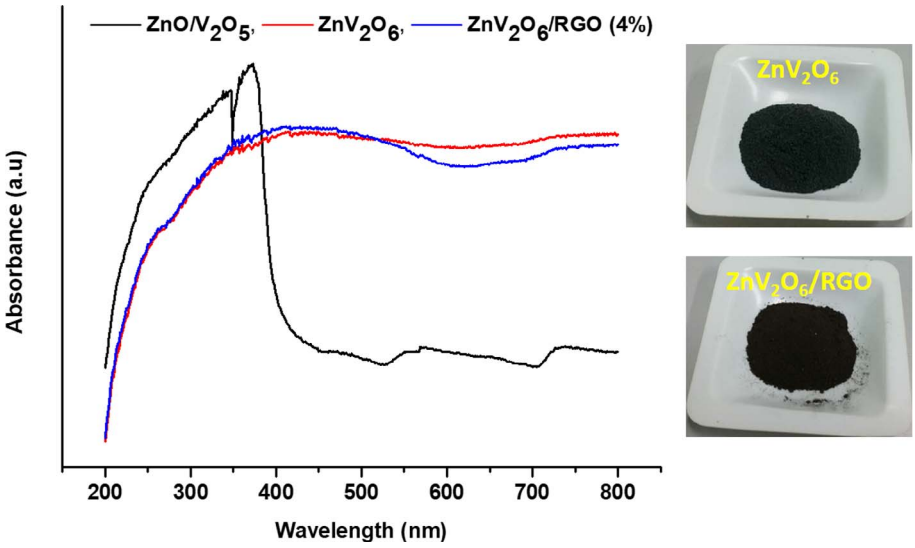

Fig. 7. UV–vis diffuse reflectance absorbance spectra of ZnO/V_2O_5 composite sample, 2D ZnV_2O_6 and 2D/2D ZnV_2O_6/RGO nanosheets.

irradiation time was probably due to some amounts of CH_3OH was initially converted to HCOOH, when there was more production of electrons at the start of the reaction [6]. In general, significantly enhanced photoactivity of RGO combined with ZnV_2O_6 nanosheets towards CO_2 reduction was evidently due to the effects of RGO for efficient separation of charges and more production of electrons over hierarchical ZnV_2O_6 nanosheets.

Fig. 10(c) shows that initially the yield of CH_3COOH production is gradually increased and then remained constant after 6 h of irradiation time. However, the amount of CH_3COOH over ZnO/V_2O_5 catalyst was significantly higher than ZnV_2O_6/RGO and ZnV_2O_6 samples. This confirms that ZnV_2O_6 nanosheets are less favourable for CH_3COOH production but has potential for selective CO_2 reduction with H_2O to CH_3OH.

The yield and selectivity of all the products is summarized in Table 2 and presented in Fig. 11. The operating parameters employed during photocatalytic CO_2 reduction with H_2O in solar photoreactor are presented in Table 3. The yield rate of CH_3OH over RGO-combined with ZnV_2O_6 catalysts is 5153.97 μmol g-cat^{-1}, 5.5-fold higher than CH_3OH yield rate over the bare ZnO/V_2O_5 and 1.6-fold higher than CH_3OH production over bare ZnV_2O_6. On the other hand, HCOOH yield rate over the ZnV_2O_6 is 2886.9 μmol g-cat^{-1}, 3.8 times higher than HCOOH yield rate over ZnO/V_2O_5 and 1.5 times higher than HCOOH yield rate over RGO-combined with ZnV_2O_6. The amount of CH_3COOH produced over ZnV_2O_6/RGO and ZnV_2O_6 were much lower than its yield over ZnO/V_2O_5 catalysts. Therefore, RGO combined with ZnV_2O_6 catalyst is efficient for the production of CH_3OH and HCOOH. Furthermore, observed CH_3OH selectivity of 39.96% over ZnO/V_2O_5 increased to 48.78% and 68.89% using ZnV_2O_6 and ZnV_2O_6/RGO samples, respectively. This significantly enhanced yield with improved selectivity towards CH_3OH reveals efficient production and utilization of electrons with suitable band structure in 2D/2D ZnV_2O_6/RGO nanosheets heterojunction.

The performance of ZnV_2O_6/RGO 2D/2D nanosheets was further compared with the results reported by previous researchers. CO_2 was converted to CH_3OH using ZnO modified reduced graphene oxide nanocomposites (ZnO-rGO) and a yield of 263.1 μmol g-cat^{-1} obtained after 3 h reaction time [39]. ZnS/MMT was used for CO_2 photo-reduction with the maximum CH_3OH yield of 3.2 μmol g-cat^{-1} after 2 h [61]. Similarly, lamellar $BiVO_4$ gave CH_3OH yield of 35 μmol g-cat^{-1} after 6 h during CO_2 photo-reduction with H_2O [62]. CdS(Bi_2S_3)/TiO_2 hetero-structure nanotubes were used to convert CO_2 to CH_3OH and reported optimum yield of 224.6 μmol g-cat^{-1} after 5 h [63]. Although, appreciable amount of CH_3OH production has been detected over different type of photo-catalysts, yet, superior yield of CH_3OH obtained in the present study using ZnV_2O_6/RGO 2D/2D nano-sheets can be attributed to the hierarchical structure with visible light absorption property and hindered charges recombination rate by RGO in 2D/2D

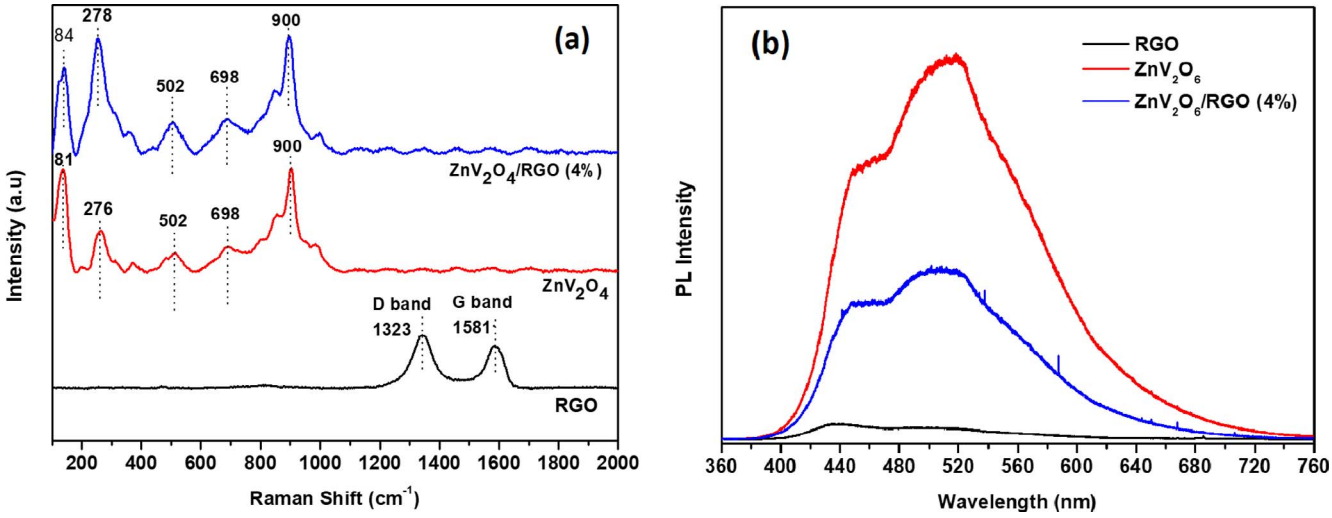

Fig. 8. (a) Raman spectra of RGO, ZnV_2O_6 and ZnV_2O_6/RGO nanosheets; (b) Photoluminescence (PL) spectra for RGO, pure ZnV_2O_6 and ZnV_2O_6/RGO nanosheets.

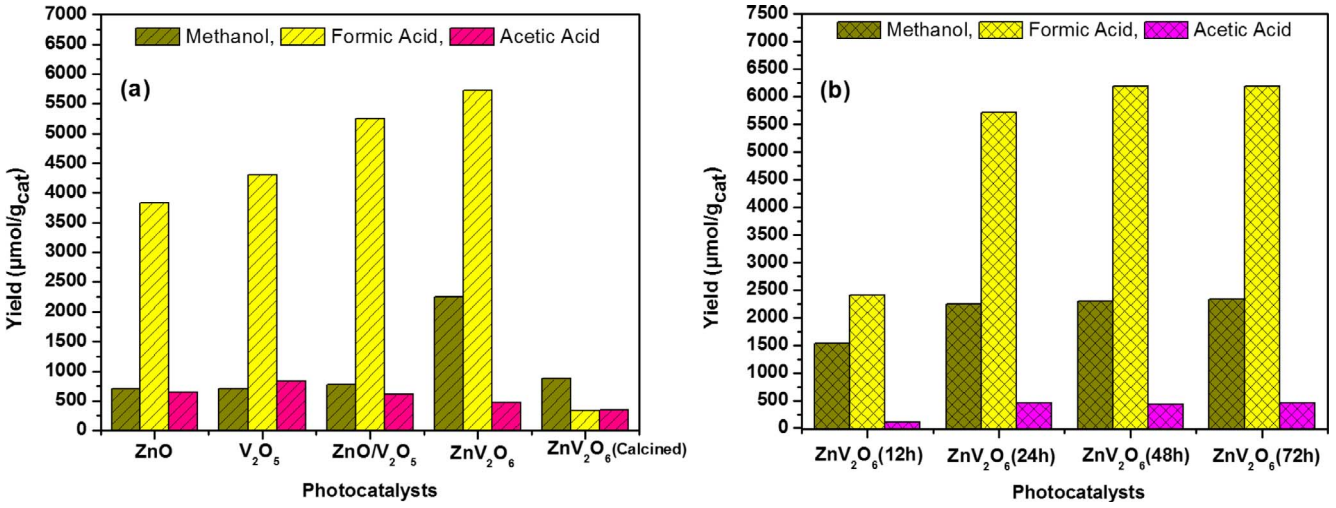

Fig. 9. (a) Effect of type of photo-catalysts on yield of methanol, formic acid and acetic acid, (b) Effect of different exposure times of heating for 12 h, 24 h, 48 h and 72 h for prepared ZnV_2O_6 catalyst for CO_2 photo-reduction with H_2O (Room temperature, atmospheric pressure, feed flow rate 20 mL/min and irradiation time = 2 h).

ZnV_2O_6/RGO hetero-structure system.

In order to check the stability of the ZnV_2O_6 and ZnV_2O_6/RGO (4%) nanosheets, a photo-stability test was performed with a cumulative of 32 h irradiation time. The effects of RGO-combined with ZnV_2O_6 for photocatalytic CO_2 reduction to CH_3OH, HCOOH and CH_3COOH using different irradiation times at room temperature, atmospheric pressure, and feed flow rate 20 mL/min are presented in Fig. 12. Evidently, over ZnV_2O_6 and ZnV_2O_6/RGO (4%), CH_3OH was observed as the main product during CO_2 photo-reduction over the entire irradiation time. The production of CH_3OH and CH_3COOH concentrations gradually increased until reached to steady state, while the yield of HCOOH was decreased significantly. At the start of the reaction, the photocatalytic CO_2 reduction into HCOOH was significantly higher in all ZnV_2O_6 and ZnV_2O_6/RGO (4%) catalysts, possibly due to initially some amount of

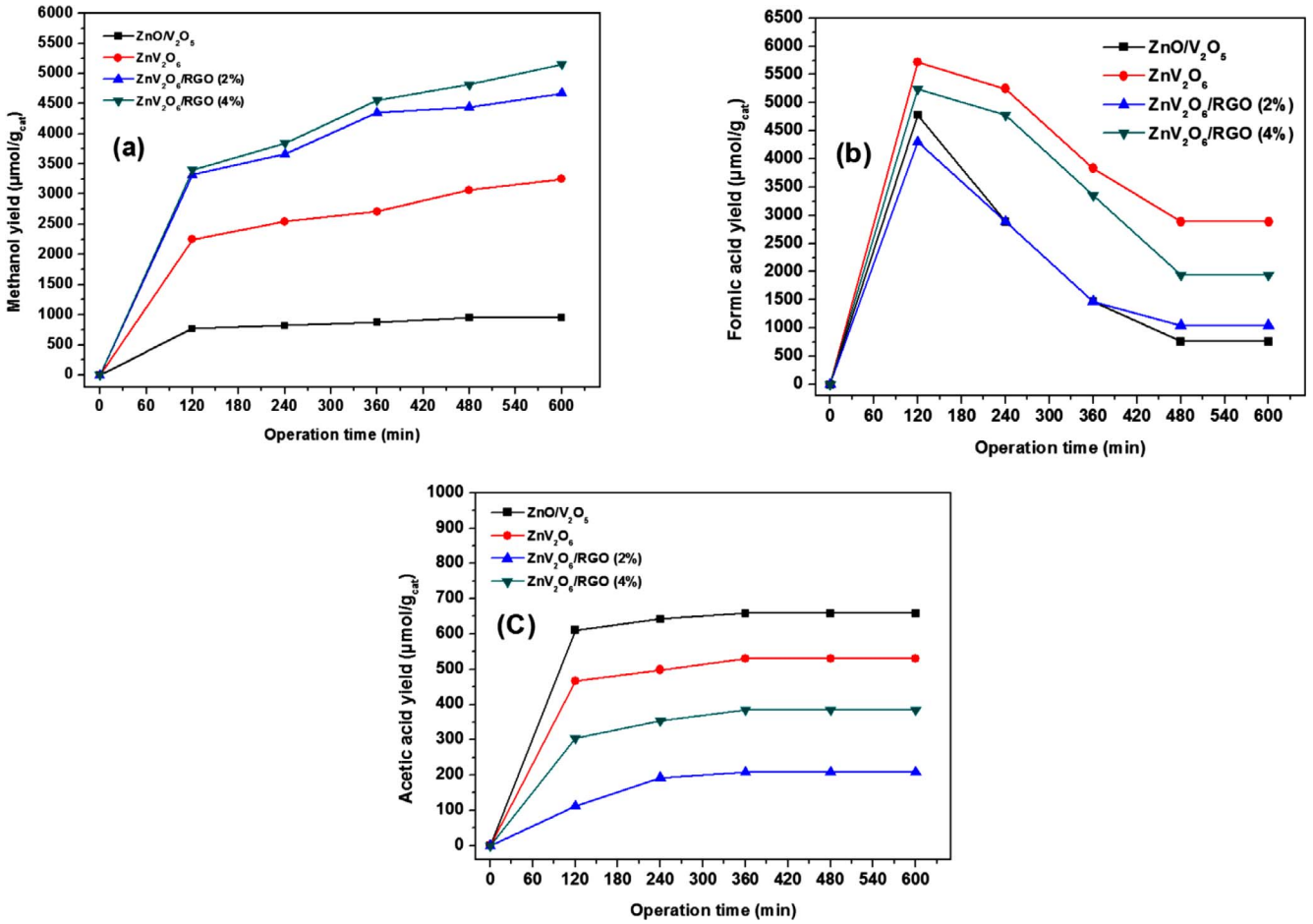

Fig. 10. Effect of RGO on the photoactivity on ZnV_2O_6 for CO_2 photo-reduction at different irradiation times: (a) methanol evolution; (b) formic acid evolution; (c) acetic acid evolution (100 mg catalyst, 100 mL distilled water with 0.1 M NaOH, room temperature, atmospheric pressure, and feed flow rate 20 mL/min).

Table 2
Summary of product yield rates during photocatalytic CO_2 reduction using different catalysts.

Catalysts	Yield of products (μmol g-cat^{-1})[a]			Selectivity (%)		
	CH_3OH	HCOOH	CH_3COOH	CH_3OH	HCOOH	CH_3COOH
ZnO/V_2O_5	945.28	761.76	658.69	39.96	32.2	27.84
ZnV_2O_6	3253.84	2886.9	530.1	48.78	43.28	7.95
4 wt% RGO/ZnV_2O_6	5153.97	1942.41	385.44	68.89	25.96	5.15

[a] Yield rates calculated at 10 h irradiation basis; parameters: 100 mg catalyst, 100 mL distilled water with 0.1 M NaOH, room temperature, atmospheric pressure, and feed flow rate 20 mL/min.

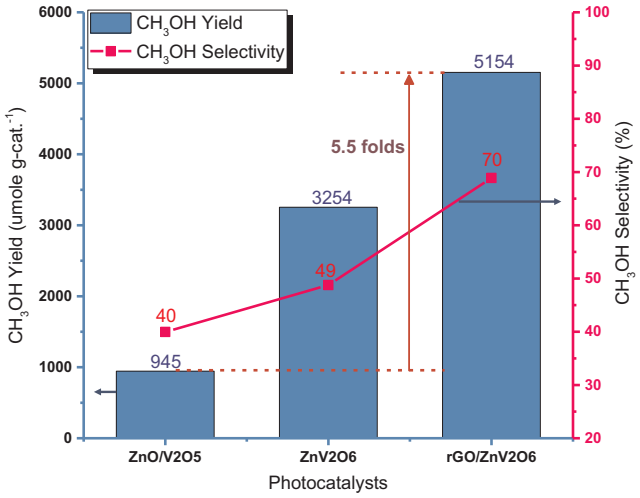

Fig. 11. Performance analysis of photo-catalysts for selective production of CH_3OH under visible light irradiations.

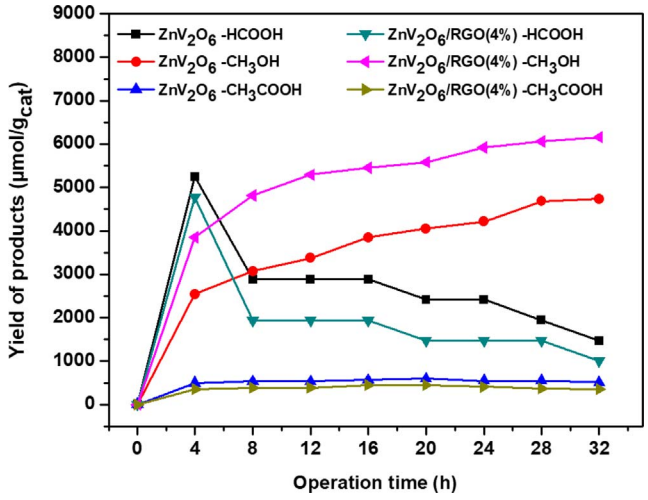

Fig. 12. Stability study under visible light irradiation of ZnV_2O_6 and ZnV_2O_6/RGO (4%) nanosheets catalyst for CO_2 reduction to CH_3OH, CH_3COO and HCOOH.

Table 3
Summary of operating parameters employed in solar type reactor.

System	ZnO/V_2O_5	ZnV_2O_6	ZnV_2O_6/4 wt% RGO
Volume	100 cm^3	100 cm^3	100 cm^3
Catalyst loading	0.1 g	0.1 g	0.1 g
Light source	35 W HID XENON	35 W HID XENON	35 W HID XENON
Temperature	Room temperature	Room temperature	Room temperature
Pressure	1 atm	1 atm	1 atm
Main products	CH_3OH, HCOOH, CH_3COOH	CH_3OH, HCOOH, CH_3COOH	CH_3OH, HCOOH, CH_3COOH
Yield rate (CH_3OH)[a] (μmol g-cat^{-1})	945.28	3253.84	5153.97

[a] Yield rates calculated at 10 h irradiation basis.

CH_3OH was converted to HCOOH, when there were more production of electrons. More importantly, catalyst sustained photo-stability even after 32 h of irradiation for selective production of CH_3OH. Therefore, novel 2D ZnV_2O_6 nano-sheets provide higher photoactivity and stability for enhanced CO_2 reduction to fuels. The addition of RGO further improved the photo-activity due to higher mobility of charges over hierarchical ZnV_2O_6 structure with hindered charges recombination rate due to their synergistic effects.

3.3. Mechanism of reaction

Pure 2D ZnV_2O_6 and ZnV_2O_6/RGO 2D/2D nanosheets are used as photocatalysts to evaluate the photocatalytic activity for photocatalytic reduction of CO_2 into CH_3OH, HCOOH and CH_3COOH. During the reduction process, the major reaction steps are described briefly in Eqs. (1)–(7).

$$ZnV_2O_6 + hv \rightarrow h^+ + e^- \quad (1)$$

$$RGO + e^- \rightarrow RGO \quad (2)$$

$$H_2O + h^+ \rightarrow \cdot OH + H^+ \quad (3)$$

$$CO_2 + e^- \rightarrow CO_2^{\cdot -} \quad (4)$$

$$CO_2 + 2H^+ + 2e^- \rightarrow HCOOH \quad (5)$$

$$CO_2 + 6H^+ + 6e^- \rightarrow CH_3OH + H_2O \quad (6)$$

$$2CO_2 + 8H^+ + 8e^- \rightarrow CH_3COOH + 2H_2O \quad (7)$$

The production of photo-excited electron-hole pairs over ZnV_2O_6 under visible light and electron trapping by RGO are listed in Eqs. (1) and (2). This leads to an increase in lifetime of charges and fosters redox reaction at the surfaces. Reduction of CO_2 occurs at the CB by the activity of electrons and H_2O is oxidized by holes at the VB and this is kinetically explained in Eqs. (3) and (4). The production of HCOOH, CH_3OH and CH_3COOH through the photo-reduction of CO_2 is shown in Eqs. (5)–(7). Based on the photoactivity and reaction pathway, insights for the reaction mechanism were obtained as shown in Fig. 13.

Under visible light irradiation, the excited electrons jump from the valence band (VB) of ZnV_2O_6 nanosheet to its conduction band (CB), but these electrons can combine with holes quickly. In ZnV_2O_6/RGO nanosheets, due to the interaction between ZnV_2O_6 nanosheet and graphene nanosheet, the electrons from ZnV_2O_6 can easily transfer to the surface of graphene and delay the combination of electron and hole. Holes in the VB of ZnV_2O_6 react with water producing O_2 and H^+. Absorbed CO_2 molecules are reduced to CH_3OH, HCOOH and CH_3COOH by enriched electrons on the graphene surface. Using ZnV_2O_6, poor photoactivity is registered attributed to higher electron-hole pairs recombination rate over the ZnV_2O_6 surface. However, production of CH_3OH was significantly enhanced using novel ZnV_2O_6/RGO

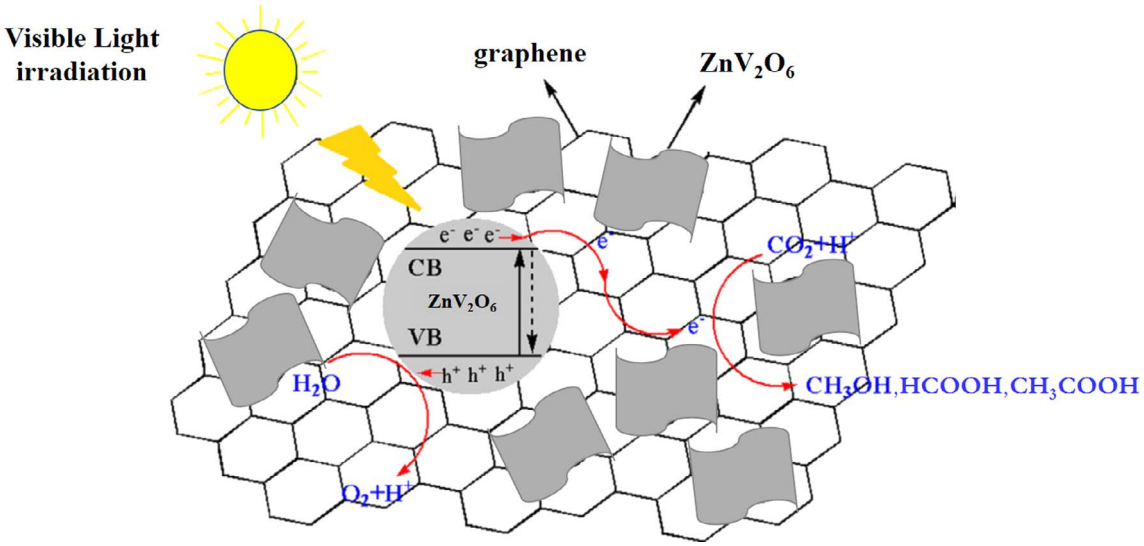

Fig. 13. Schematic presentation of charge separation and transfer in the ZnV_2O_6/RGO system for photo-reduction of CO_2 to CH_3OH, HCOOH and CH_3COOH under visible light.

2D/2D nanosheets due to synergistic effects, efficient visible light absorption, appropriate band structure and higher electron mobility with hindered recombination rate.

4. Conclusions

The novel 2D ZnV_2O_6 nanosheets combining with 2D RGO successfully synthesized to get 2D/2D nanosheets heterojunction with hindered charges recombination rate and enhanced photocatalytic CO_2 reduction with H_2O to CH_3OH, HCOOH and CH_3COOH. More importantly, hierarchical structure of ZnV_2O_6 favoured selective CH_3OH production under visible light irradiation. Yield rate of CH_3OH as the main product over ZnV_2O_6/4.0 wt% RGO catalyst was 5154 μmol $g\text{-}cat^{-1}$, significantly higher than using ZnV_2O_6 and ZnO/V_2O_5 under visible light irradiation. The observed CH_3OH selectivity of 39.96% over ZnO/V_2O_5 increased to 68.89% using ZnV_2O_6/RGO sample, respectively. The enhanced photocatalytic activity was attributed to hierarchical structure of ZnV_2O_6 with hindered charges recombination rate by RGO. The stability test revealed, ZnV_2O_6 based catalysts sustained photoactivity and selectivity even after 32 h of irradiation time. The finding of this work could be useful to develop an efficient solar system for selective photo-catalytic CO_2 reduction to valuable chemicals and fuels.

Acknowledgements

The authors would like to extend their deepest appreciation to Ministry of Higher Education (MOHE) Malaysia for financial support of this research under FRGS (Fundamental Research Grant Scheme, Vot 4F876) and University Technology Malaysia (UTM), Malaysia for financial support of this research under Tire 1 (Research University Grant Scheme, Vot 17H06).

References

[1] M. Tahir, Photocatalytic carbon dioxide reduction to fuels in continuous flow monolith photoreactor using montmorillonite dispersed Fe/TiO_2 nanocatalyst, J. Cleaner Prod. 170 (2017) 242–250.
[2] Y. Tong, L. Chen, S. Ning, N. Tong, Z. Zhang, H. Lin, F. Li, X. Wang, Photocatalytic reduction of CO_2 to CO over the Ti–Highly dispersed HZSM-5 zeolite containing Fe, Appl. Catal., B 203 (2017) 725–730.
[3] E.V. Kondratenko, G. Mul, J. Baltrusaitis, G.O. Larrazábal, J. Pérez-Ramírez, Status and perspectives of CO_2 conversion into fuels and chemicals by catalytic, photocatalytic and electrocatalytic processes, Energy Environ. Sci. 6 (2013) 3112.
[4] G. Centi, E.A. Quadrelli, S. Perathoner, Catalysis for CO_2 conversion: a key technology for rapid introduction of renewable energy in the value chain of chemical industries, Energy Environ. Sci. 6 (2013) 1711.
[5] N. Wang, S. Yan, Z. Zou, Photoreduction of CO_2 into hydrocarbons catalysed by $ZnGa_2O_4/Ga_2O_3$ heterojunction, Curr. Org. Chem. 17 (2013) 2454–2458.
[6] M. Tahir, B. Tahir, N.A.S. Amin, Z.Y. Zakaria, Photo-induced reduction of CO_2 to CO with hydrogen over plasmonic Ag-NPs/TiO_2 NWs core/shell hetero-junction under UV and visible light, J. CO_2 Util. 18 (2017) 250–260.
[7] M. Tahir, N.S. Amin, Photocatalytic CO_2 reduction with H_2O vapors using montmorillonite/TiO_2 supported microchannel monolith photoreactor, Chem. Eng. J. 230 (2013) 314–327.
[8] M. Tahir, Synergistic effect in MMT-dispersed Au/TiO_2 monolithic nanocatalyst for plasmon-absorption and metallic interband transitions dynamic CO_2 photo-reduction to CO, Appl. Catal., B 219 (2017) 329–343.
[9] Y. Liu, B. Huang, Y. Dai, X. Zhang, X. Qin, M. Jiang, M.-H. Whangbo, Selective ethanol formation from photocatalytic reduction of carbon dioxide in water with $BiVO_4$ photocatalyst, Catal. Commun. 11 (2009) 210–213.
[10] M. Tahir, B. Tahir, N.A.S. Amin, Synergistic effect in plasmonic Au/Ag alloy NPs co-coated TiO_2 NWs toward visible-light enhanced CO_2 photoreduction to fuels, Appl. Catal., B 204 (2017) 548–560.
[11] W. Fan, Q. Zhang, Y. Wang, Semiconductor-based nanocomposites for photocatalytic H_2 production and CO_2 conversion, Phys. Chem. Chem. Phys. 15 (2013) 2632–2649.
[12] J. Mao, K. Li, T. Peng, Recent advances in the photocatalytic CO_2 reduction over semiconductors, Catal. Sci. Technol. 3 (2013) 2481.
[13] J. Yu, J. Jin, B. Cheng, M. Jaroniec, A noble metal-free reduced graphene oxide–CdS nanorod composite for the enhanced visible-light photocatalytic reduction of CO_2 to solar fuel, J. Mater. Chem. A 2 (2014) 3407.
[14] E. Liu, L. Kang, F. Wu, T. Sun, X. Hu, Y. Yang, H. Liu, J. Fan, Photocatalytic reduction of CO_2 into methanol over Ag/TiO_2 nanocomposites enhanced by surface plasmon resonance, Plasmonics 9 (2013) 61–70.
[15] H. Xu, S. Ouyang, P. Li, T. Kako, J. Ye, High-active anatase TiO_2 nanosheets exposed with 95%{100} facets toward efficient H_2 evolution and CO_2 photoreduction, ACS Appl. Mater. Interfaces 5 (2013) 1348–1354.
[16] Q. Wang, W. Wang, B. Yan, W. Shi, F. Cui, C. Wang, Well-dispersed Pd-Cu bimetals in TiO_2 nanofiber matrix with enhanced activity and selectivity for nitrate catalytic reduction, Chem. Eng. J. 326 (2017) 182–191.
[17] M.M. Gui, W.M.P. Wong, S.P. Chai, A.R. Mohamed, One-pot synthesis of Ag-MWCNT@TiO_2 core-shell nanocomposites for photocatalytic reduction of CO_2 with water under visible light irradiation, Chem. Eng. J. 278 (2015) 272–278.
[18] G. Mahmodi, S. Sharifnia, F. Rahimpour, S.N. Hosseini, Photocatalytic conversion of CO_2 and CH_4 using ZnO coated mesh: effect of operational parameters and optimization, Sol. Energy Mater. Sol. Cells 111 (2013) 31–40.
[19] A. Moezzi, A.M. McDonagh, M.B. Cortie, Zinc oxide particles: synthesis, properties and applications, Chem. Eng. J. 185 (2012) 1–22.
[20] Y.S. Chaudhary, T.W. Woolerton, C.S. Allen, J.H. Warner, E. Pierce, S.W. Ragsdale, F.A. Armstrong, Visible light-driven CO_2 reduction by enzyme coupled CdS nanocrystals, Chem. Commun. (Camb) 48 (2012) 58–60.
[21] T.M. Suzuki, T. Nakamura, S. Saeki, Y. Matsuoka, H. Tanaka, K. Yano, T. Kajino, T. Morikawa, Visible light-sensitive mesoporous N-doped Ta_2O_5 spheres: synthesis and photocatalytic activity for hydrogen evolution and CO_2 reduction, J. Mater. Chem. 22 (2012) 24584.
[22] C.-W. Tsai, H.M. Chen, R.-S. Liu, K. Asakura, T.-S. Chan, Ni@ NiO core–shell structure-modified nitrogen-doped InTaO4 for solar-driven highly efficient CO_2 reduction to methanol, J. Phys. Chem. C 115 (2011) 10180–10186.
[23] L. Vayssieres, Growth of arrayed nanorods and nanowires of ZnO from aqueous solutions, Adv. Mater. 15 (2003) 464–466.
[24] C. Tian, Q. Zhang, A. Wu, M. Jiang, Z. Liang, B. Jiang, H. Fu, Cost-effective large-scale synthesis of ZnO photocatalyst with excellent performance for dye

photodegradation, Chem. Commun. 48 (2012) 2858–2860.
[25] L. Collado, P. Jana, B. Sierra, J.M. Coronado, P. Pizarro, D.P. Serrano, V.A. de la Peña O'Shea, Enhancement of hydrocarbon production via artificial photosynthesis due to synergetic effect of Ag supported on TiO_2 and ZnO semiconductors, Chem. Eng. J. 224 (2013) 128–135.
[26] J. Wang, W.-D. Zhang, W.-X. Ouyang, Y.-X. Yu, Hierarchically branched ZnO/CuO thin film with enhanced visible light photoelectrochemical property, Mater. Lett. 154 (2015) 44–46.
[27] K. Kočí, L. Matějová, O. Kozák, L. Čapek, V. Valeš, M. Reli, P. Praus, K. Šafářová, A. Kotarba, L. Obalová, ZnS/MMT nanocomposites: the effect of ZnS loading in MMT on the photocatalytic reduction of carbon dioxide, Appl. Catal., B 158-159 (2014) 410–417.
[28] R. Khan, M.S. Hassan, L.-W. Jang, J. Hyeon Yun, H.-K. Ahn, M.-S. Khil, I.-H. Lee, Low-temperature synthesis of ZnO quantum dots for photocatalytic degradation of methyl orange dye under UV irradiation, Ceram. Int. 40 (2014) 14827–14831.
[29] C. Yu, K. Yang, Y. Xie, Q. Fan, J.C. Yu, Q. Shu, C. Wang, Novel hollow Pt-ZnO nanocomposite microspheres with hierarchical structure and enhanced photocatalytic activity and stability, Nanoscale 5 (2013) 2142–2151.
[30] M. Pirhashemi, A. Habibi-Yangjeh, Ultrasonic-assisted preparation of plasmonic ZnO/Ag/Ag_2WO_4 nanocomposites with high visible-light photocatalytic performance for degradation of organic pollutants, J. Colloid. Interface Sci. 491 (2017) 216–229.
[31] M. Pirhashemi, A. Habibi-Yangjeh, Preparation of novel nanocomposites by deposition of Ag_2WO_4 and AgI over ZnO particles: efficient plasmonic visible-light-driven photocatalysts through a cascade mechanism, Ceram. Int. 43 (2017) 13447–13460.
[32] A. Yarahmadi, S. Sharifnia, Dye photosensitization of ZnO with metallophthalocyanines (Co, Ni and Cu) in photocatalytic conversion of greenhouse gases, Dyes Pigm. 107 (2014) 140–145.
[33] C.S. Chen, T.G. Liu, L.W. Lin, X.D. Xie, X.H. Chen, Q.C. Liu, B. Liang, W.W. Yu, C.Y. Qiu, Multi-walled carbon nanotube-supported metal-doped ZnO nanoparticles and their photocatalytic property, J. Nanopart. Res. 15 (2013) 1295.
[34] X. Li, Q. Wang, Y. Zhao, W. Wu, J. Chen, H. Meng, Green synthesis and photocatalytic performances for ZnO-reduced graphene oxide nanocomposites, J. Colloid Interface Sci. 411 (2013) 69–75.
[35] A. Habibi-Yangjeh, M. Shekofteh-Gohari, Novel magnetic Fe_3O_4/ZnO/$NiWO_4$ nanocomposites: Enhanced visible-light photocatalytic performance through pn heterojunctions, Sep. Purif. Technol. 184 (2017) 334–346.
[36] M. Shekofteh-Gohari, A. Habibi-Yangjeh, Fe_3O_3/ZnO/$CoWO_4$ nanocomposites: novel magnetically separable visible-light-driven photocatalysts with enhanced activity in degradation of different dye pollutants, Ceram. Int. 43 (2017) 3063–3071.
[37] K. Ullah, S. Ye, L. Zhu, S.B. Jo, W.K. Jang, K.-Y. Cho, W.-C. Oh, Noble metal doped graphene nanocomposites and its study of photocatalytic hydrogen evolution, Solid State Sci. 31 (2014) 91–98.
[38] J. Ke, X. Duan, S. Luo, H. Zhang, H. Sun, J. Liu, M. Tade, S. Wang, UV-assisted construction of 3D hierarchical rGO/Bi_2MoO_6 composites for enhanced photocatalytic water oxidation, Chem. Eng. J. 313 (2017) 1447–1453.
[39] L. Zhang, N. Li, H. Jiu, G. Qi, Y. Huang, ZnO-reduced graphene oxide nanocomposites as efficient photocatalysts for photocatalytic reduction of CO_2, Ceram. Int. 41 (2015) 6256–6262.
[40] L.-L. Tan, W.-J. Ong, S.-P. Chai, A.R. Mohamed, Reduced graphene oxide-TiO_2 nanocomposite as a promising visible-light-active photocatalyst for the conversion of carbon dioxide, Nanoscale Res. Lett. 8 (2013) 465.
[41] P.-Q. Wang, Y. Bai, P.-Y. Luo, J.-Y. Liu, Graphene–WO_3 nanobelt composite: elevated conduction band toward photocatalytic reduction of CO_2 into hydrocarbon fuels, Catal. Commun. 38 (2013) 82–85.
[42] R. Akbarzadeh, S.B. Umbarkar, R.S. Sonawane, S. Takle, M.K. Dongare, Vanadia–titania thin films for photocatalytic degradation of formaldehyde in sunlight, Appl. Catal., A 374 (2010) 103–109.
[43] J. Su, X.-X. Zou, G.-D. Li, X. Wei, C. Yan, Y.-N. Wang, J. Zhao, L.-J. Zhou, J.-S. Chen, Macroporous V_2O_5 – $BiVO_4$ composites: effect of heterojunction on the behavior of photogenerated charges, J. Phys. Chem. C 115 (2011) 8064–8071.
[44] F.K. Butt, M. Tahir, C. Cao, F. Idrees, R. Ahmed, W.S. Khan, Z. Ali, N. Mahmood, M. Tanveer, A. Mahmood, Synthesis of novel ZnV_2O_4 hierarchical nanospheres and their applications as electrochemical supercapacitor and hydrogen storage material, ACS Appl. Mater. Interfaces 6 (2014) 13635–13641.
[45] Y. Shi, C. Zhu, L. Wang, C. Zhao, W. Li, K.K. Fung, T. Ma, A. Hagfeldt, N. Wang, Ultrarapid sonochemical synthesis of ZnO hierarchical structures: from fundamental research to high efficiencies up to 6.42% for quasi-solid dye-sensitized solar cells, Chem. Mater. 25 (2013) 1000–1012.
[46] F.K. Butt, C. Cao, Q. Wan, P. Li, F. Idrees, M. Tahir, W.S. Khan, Z. Ali, M.J. Zapata, M. Safdar, Synthesis, evolution and hydrogen storage properties of ZnV_2O_4 glomerulus nano/microspheres: a prospective material for energy storage, Int. J. Hydrogen Energy 39 (2014) 7842–7851.
[47] L. Xiao, Y. Zhao, J. Yin, L. Zhang, Clewlike ZnV_2O_4 hollow spheres: nonaqueous sol–gel synthesis, formation mechanism, and lithium storage properties, Chem. Eur. J. 15 (2009) 9442–9450.
[48] F.K. Butt, C. Cao, R. Ahmed, W.S. Khan, T. Cao, N. Bidin, P. Li, Q. Wan, X. Qu, M. Tahir, Synthesis of novel ZnV_2O_4 spinel oxide nanosheets and their hydrogen storage properties, CrystEngComm 16 (2014) 894–899.
[49] F. Duan, W. Dong, D. Shi, M. Chen, Template-free synthesis of ZnV_2O_4 hollow spheres and their application for organic dye removal, Appl. Surf. Sci. 258 (2011) 189–195.
[50] H. Wang, L. Zhang, Z. Chen, J. Hu, S. Li, Z. Wang, J. Liu, X. Wang, Semiconductor heterojunction photocatalysts: design, construction, and photocatalytic performances, Chem. Soc. Rev. 43 (2014) 5234–5244.
[51] E. Gao, W. Wang, M. Shang, J. Xu, Synthesis and enhanced photocatalytic performance of graphene-Bi_2WO_6 composite, PCCP 13 (2011) 2887–2893.
[52] P. Kumar, C. Joshi, A. Barras, B. Sieber, A. Addad, L. Boussekey, S. Szunerits, R. Boukherroub, S.L. Jain, Core–shell structured reduced graphene oxide wrapped magnetically separable rGO@CuZnO@Fe_3O_4 microspheres as superior photocatalyst for CO_2 reduction under visible light, Appl. Catal., B 205 (2017) 654–665.
[53] S. Tonda, S. Kumar, Y. Gawli, M. Bhardwaj, S. Ogale, g-C_3N_4 (2D)/CdS (1D)/rGO (2D) dual-interface nano-composite for excellent and stable visible light photocatalytic hydrogen generation, Int. J. Hydrogen Energy 42 (2017) 5971–5984.
[54] Z. Yin, J. Qin, W. Wang, M. Cao, Rationally designed hollow precursor-derived $Zn_3V_2O_8$ nanocages as a high-performance anode material for lithium-ion batteries, Nano Energy 31 (2017) 367–376.
[55] T. Zhang, Y. Shen, Y.-H. Qiu, Y. Liu, R. Xiong, J. Shi, J. Wei, Facial synthesis and photoreaction mechanism of $BiFeO_3$/$Bi_2Fe_4O_9$ heterojunction nanofibers, ACS Sustainable Chem. Eng. 5 (2017) 4630–4636.
[56] H.A. Almukhlifi, R.C. Burns, Oxidative dehydrogenation of isobutane to isobutene by pyrovanadates, M2V2O7, where M(II) = Mn Co, Ni, Cu and Zn, and Co_2VO_4 and ZnV_2O_4: The effect of gold nanoparticles, J. Mol. Catal. A: Chem. 408 (2015) 26–40.
[57] J. Xu, W. Wang, S. Sun, L. Wang, Enhancing visible-light-induced photocatalytic activity by coupling with wide-band-gap semiconductor: a case study on Bi_2WO_6/TiO_2, Appl. Catal., B 111 (2012) 126–132.
[58] S.-M. Chang, W.-S. Liu, Surface doping is more beneficial than bulk doping to the photocatalytic activity of vanadium-doped TiO_2, Appl. Catal., B 101 (2011) 333–342.
[59] Z. Chen, N. Zhang, Y.-J. Xu, Synthesis of graphene–ZnO nanorod nanocomposites with improved photoactivity and anti-photocorrosion, CrystEngComm 15 (2013) 3022.
[60] J. He, C. Niu, C. Yang, J. Wang, X. Su, Reduced graphene oxide anchored with zinc oxide nanoparticles with enhanced photocatalytic activity and gas sensing properties, RSC Adv. 4 (2014) 60253–60259.
[61] K. Kočí, M. Reli, O. Kozák, Z. Lacný, D. Plachá, P. Praus, L. Obalová, Influence of reactor geometry on the yield of CO 2 photocatalytic reduction, Catal. Today 176 (2011) 212–214.
[62] J. Mao, T. Peng, X. Zhang, K. Li, L. Zan, Selective methanol production from photocatalytic reduction of CO_2 on $BiVO_4$ under visible light irradiation, Catal. Commun. 28 (2012) 38–41.
[63] X. Li, H. Liu, D. Luo, J. Li, Y. Huang, H. Li, Y. Fang, Y. Xu, L. Zhu, Adsorption of CO_2 on heterostructure CdS (Bi_2S_3)/TiO_2 nanotube photocatalysts and their photocatalytic activities in the reduction of CO_2 to methanol under visible light irradiation, Chem. Eng. J. 180 (2012) 151–158.